

# Growth of shear failure in snow slab avalanche release: analytical solution for a compliant weak layer with finite softening

Johan Gaume<sup>1,2,3</sup>, Francis Meloche<sup>1,2,3</sup>, and Ingrid Reiweger<sup>4</sup>

<sup>1</sup>*Institute for Geotechnical Engineering, ETH Zürich, Zürich, Switzerland*

<sup>2</sup>*WSL Institute for Snow and Avalanche Research SLF, Davos, Switzerland*

<sup>3</sup>*Climate Change, Extremes and Natural Hazards in Alpine Regions Research Center (CERC), Davos, Switzerland*

<sup>4</sup>*Institute of Mountain Risk Engineering, Department of Landscape, Water and Infrastructure, BOKU University of Natural Resources and Life Sciences, 1180 Vienna, Austria*

May 7, 2026

## Abstract

Snow slab avalanches are among the most dangerous natural hazards in mountain regions. They are responsible for most avalanche accidents and fatalities among recreationists, while large events can also threaten settlements and infrastructure, with potentially severe consequences for human lives. Recent progress in numerical modelling, field measurements, and large-scale fracture experiments has renewed interest in shear-failure interpretations of avalanche release, particularly in connection with dynamic crack propagation and supershear fracture. Yet, most existing stress-based models of weak-layer shear failure either assume a perfectly brittle stress drop from peak strength to residual friction, thereby neglecting the energy dissipated during post-peak softening, or neglect the pre-peak elastic response of the weak layer, which can strongly influence stress redistribution and the resulting critical crack length.

Here, we derive an analytical solution for shear failure propagation in a weak layer buried beneath an elastic snow slab, explicitly accounting for finite post-peak softening and for the elastic mismatch between the slab and the weak layer. Building on the one-dimensional weak-spot framework of Gaume et al. [2013], we consider a symmetric failure composed of a fully softened zone at residual strength, a fracture process zone with linear softening, and an intact elastic region. In the limit of vanishing softening displacement  $\delta$ , the model recovers the classical stress-based critical length  $a_{c0}$ . For finite softening, the solution distinguishes between the fully softened crack length  $a_c$  and the total affected length  $b_c$ , which also includes the fracture process zone. This distinction is essential for comparison with numerical models, which may measure the complete damaged region rather than the fully softened zone alone.

The presented model formulation provides a direct analytical link between stress-based weak-spot approaches and fracture-energy concepts, since the fracture-energy contribution enters through the constitutive softening law rather than through an externally imposed propagation criterion. For small softening, the exact solution yields a compact approximation for the fully softened crack length,  $a_c \simeq a_{c0} \sqrt{1 + C_a \delta / u_p}$  while the fracture-process-zone length grows linearly with the softening displacement,  $\omega \propto \Lambda \frac{\delta}{u_p}$ . The total affected length then follows as  $b_c = a_c + \omega$ , where  $u_p$  is the displacement at peak strength and  $C_a$  and  $C_b$  are dimensionless coefficients determined by the peak, residual, and gravitational shear stresses and  $\Lambda$  is the characteristic elastic length of the system.

Finally, we discuss how the same three-zone reasoning can be extended to the onset of anticrack propagation. In this case, slab bending introduces a distinct bending-controlled length scale proportional to  $\delta^{1/4}$ , in contrast to the  $\delta^{1/2}$  scaling of the shear problem. The corresponding compressive anticrack analogue admits an exact three-zone analytical reduction, although it does not reduce to a compact scalar expression comparable to the shear case. Three-dimensional MPM simulations support the resulting quarter-power dependence of the anticrack lengths on the compressive softening distance.

# 1 Introduction

Snow slab avalanche release is commonly described as a fracture process occurring in a weak snow layer buried beneath a cohesive slab. Although many modern theories emphasize weak-layer collapse and anticrack propagation, the first analytical framework for snow slab avalanche release was fundamentally shear-based. Inspired by Palmer and Rice [1973], McClung [1979] formulated the onset of crack propagation as the unstable extension of a shear band in a strain-softening weak layer, introducing the key idea that post-peak weakening provides the mechanical driving mechanism for release. This approach established a direct link between weak-layer strength, softening, slab load, and critical crack length. Related shear-based models were later developed by Chiaia et al. [2008] and Gaume et al. [2013], the latter also including residual friction. However, these models not only neglected weak-layer elasticity, thereby leading to the unrealistic prediction of a zero critical crack length in the limit of vanishing softening distance, or fracture toughness, but also failed to explain key field observations such as remote triggering, whumpfs, and crack propagation on flat or low-angle terrain.

The latter limitation motivated the anticrack theory of Heierli et al. [2008], in which weak-layer collapse induces slab bending and drives a compressive fracture with the closure of the crack faces. This anticrack framework successfully explained several observations that were difficult to reconcile with shear-only models and strongly influenced subsequent analytical and numerical work. The anticrack concept was later incorporated into numerous numerical models. In particular, the finite-element models of Mahajan et al. [2010], Volmer et al. [2017] and the discrete-element simulations of Gaume et al. [2015, 2017], Bobillier et al. [2024] highlighted the importance of weak-layer collapse, slab bending, and mixed-mode fracture processes in governing both the onset and the subsequent dynamics of crack propagation. These studies progressively shifted much of the theoretical interpretation of slab avalanche release from a purely shear-driven instability toward a collapse-driven anticrack mechanism. More recently, efficient closed-form analytical models were introduced by Rosendahl and Weissgraeber [2020a,b]. These approaches capture not only failure initiation but also the onset of crack propagation, including the effects of layering in the overlying slab [Weissgraeber and Rosendahl, 2023], overcoming the limitations of previous effective-stiffness models [Monti et al., 2016].

However, recent work has shown that shear-based mechanisms remain essential, especially on steep slopes and at large propagation distances. Numerical simulations by Trottet et al. [2021] demonstrated a transition from sub-Rayleigh anticrack propagation to supershear crack propagation on slopes, indicating that once dynamic propagation is established, weak-layer collapse and slab bending may become secondary, with propagation then primarily driven by shear failure in the weak layer. This interpretation was further explored by Guillet et al. [2023], Meloche et al. [2025], who used a depth-averaged Material Point Method (MPM) with a weak-layer shear-softening interface to study the onset and dynamics of crack propagation, crack arrest, and avalanche release size at slope scale. In parallel, Siron et al. [2023] provided a theoretical framework for dynamic crack propagation regimes, extending the unbounded theory of Heierli [2008] while explicitly incorporating weak-layer properties.

These recent developments bring renewed relevance to McClung [1979]’s original shear concept. They suggest that although weak-layer collapse is crucial for crack nucleation and anticrack propagation on flat or low-angle terrain and during the early stages of crack propagation on slopes, the dynamics of large slab avalanches on steep slopes may be governed to first order by shear failure and softening in the weak layer. The objective of the present paper is therefore to revisit softening shear-based theory within a modern analytical framework that extends McClung [1979]’s model to a situation in which the elastic mismatch between the slab and the weak layer is considered. By explicitly accounting for weak-layer compliance and post-peak weakening, we derive a comprehensive analytical model that connects weak-layer and slab mechanical properties to the onset of crack propagation. The resulting formulation provides a mechanics-based criterion for evaluating crack propagation propensity in a slab–weak-layer system, while

accounting for weak-layer elasticity, strength, residual friction, and fracture energy through the constitutive softening law itself.

## 2 Analytical model

We first note that, for clarity, we use the notation  $a_c$  to denote the critical crack length for the onset of crack propagation in a slab–weak-layer system, regardless of the assumed failure mode of the weak layer. Strictly speaking, in the case of weak-layer shear failure, and in light of recent numerical, theoretical, and experimental work, this length would more appropriately be referred to as the *supercritical crack length*  $a_{sc}$ , following Trottet et al. [2021] and Meloche et al. [2025]. However, to avoid introducing multiple notations, we deliberately retain the simpler notation  $a_c$  throughout this paper. In the Discussion section, where we briefly extend the analysis to the onset of crack propagation under mixed-mode anticrack conditions, we continue to use the same notation for consistency.

### 2.1 Mechanical framework

We consider a one-dimensional slab–weak-layer system following the framework of Gaume et al. [2013], extended to include a finite post-peak softening displacement (Figure 1). The snow slab is modeled as a linear elastic layer of thickness  $h$ , and deformation is assumed to occur only in the slope-parallel direction  $x$ . We use a Cartesian coordinate system in which  $x$  is oriented slope-parallel and  $z$  is positive upward, with  $z = 0$  at the free surface of the slab and  $z = -h$  at the slab–weak-layer interface. The gravitational loading is represented by a uniform shear stress  $\tau_g$ , while the weak layer is represented as a shear interface transmitting a stress  $\tau(x)$ . Stress redistribution along the weak layer is therefore governed by the axial elasticity of the overlying slab.

The slope-parallel equilibrium of a slab element can be written in integrated form as

$$\frac{\partial}{\partial x} \left( \int_{-h}^0 \sigma_{xx} dz \right) - \tau(x) = -\tau_g, \quad (1)$$

where  $\sigma_{xx}$  is the slope-parallel normal stress in the slab. Under the one-dimensional elastic approximation, the depth-integrated ( $z$ -direction) axial force is related to the weak-layer displacement  $u(x)$  through

$$\int_{-h}^0 \sigma_{xx} dz \simeq E' h u'(x),$$

where  $E'$  is the plane-strain elastic modulus. The governing equation is therefore

$$E' h u''(x) - \tau(x) = -\tau_g. \quad (2)$$

Here and in the following, primes denote derivatives with respect to the slope-parallel coordinate  $x$ , i.e.  $u' = du/dx$  and  $u'' = d^2u/dx^2$ .

### 2.2 Weak-layer interface law

The weak layer is described by a local shear stress–displacement law with finite post-peak softening (Figure 1b). The response is linear elastic up to a peak shear stress  $\tau_p$ , reached at displacement  $u_p$ . It then softens linearly until the residual shear stress  $\tau_r$  is reached at displacement  $u_r$ . The softening displacement is

$$\delta = u_r - u_p \geq 0. \quad (3)$$

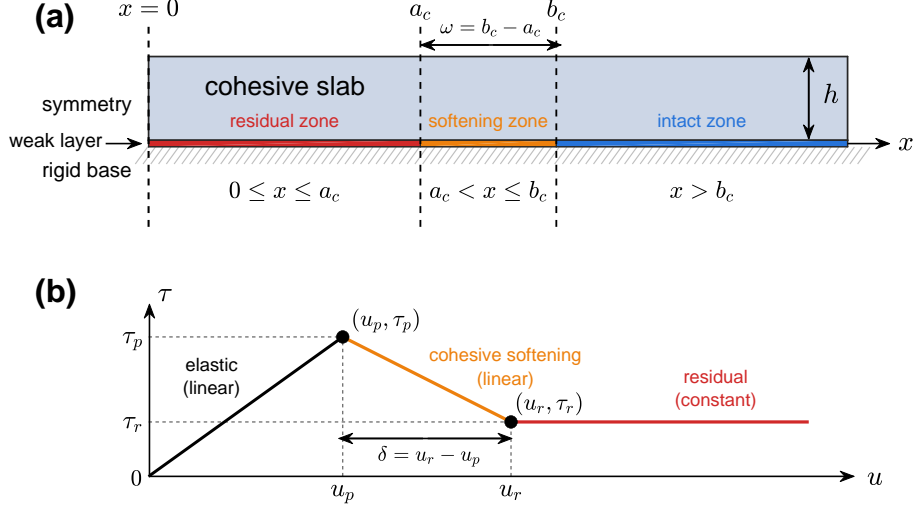


Figure 1: Slab–weak layer system geometry and weak-layer constitutive model.

The interface law reads

$$\tau(u) = \begin{cases} \frac{\tau_p}{u_p} u, & 0 \leq u \leq u_p, \\ \tau_p - \frac{\tau_p - \tau_r}{\delta} (u - u_p), & u_p \leq u \leq u_r, \\ \tau_r, & u \geq u_r. \end{cases} \quad (4)$$

This law provides a minimal representation of weak-layer weakening. The parameter  $u_p$  controls the initial elastic stiffness,  $\delta$  controls the softening distance, and  $\tau_r$  represents the residual shear resistance after complete local softening.

### 2.3 Three-zone structure

We seek a symmetric solution around  $x = 0$  and therefore consider only the half-domain  $x \geq 0$ . The solution consists of three regions. Closest to  $x = 0$ , the weak layer is fully softened and carries only the residual shear stress  $\tau_r$ . This residual zone occupies

$$0 \leq x \leq a_c.$$

Ahead of it lies a softening, or fracture process zone, in which the displacement decreases from  $u_r$  to  $u_p$  and the stress follows the softening branch of Eq. (4). This zone occupies

$$a_c \leq x \leq b_c.$$

Finally, for  $x \geq b_c$ , the weak layer remains intact and follows the elastic branch.

The softening zone length is denoted by

$$\omega = b_c - a_c. \quad (5)$$

Thus,  $a_c$  is the fully residual half-length, whereas  $b_c$  is the total affected half-length, including both the residual and softening zones. Symmetry imposes

$$u'(0) = 0. \quad (6)$$

The symmetry assumption makes the problem equivalent to one half of a centered weak-spot configuration, rather than to the open-ended PST geometry commonly used in the field.

The system geometry and associated zones as well as the weak layer interface constitutive model are shown in Fig. 1.

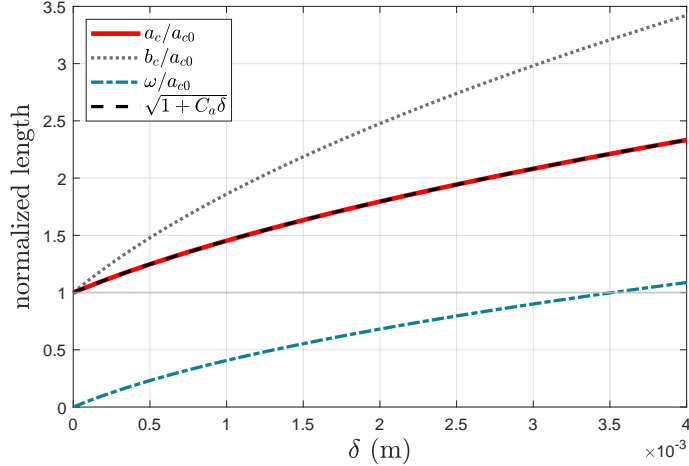


Figure 2: Normalized characteristic lengths as a function of the softening displacement  $\delta$ . The critical crack length  $a_c$ , the critical propagation length  $b_c$ , and the softening zone length  $\omega = b_c - a_c$  are normalized by the brittle critical length  $a_{c0}$ . The dashed curve shows the small-softening square-root approximation for  $a_c/a_{c0}$ , given by  $\sqrt{1 + C_a \delta/u_p}$ . The results illustrate that finite softening modifies the fully softened crack length and introduces a finite process zone, so that the critical propagation length  $b_c$  exceeds the critical crack length  $a_c$ .

### 3 Exact solution

#### 3.1 Characteristic lengths

The solution involves two characteristic lengths. The first is the elastic characteristic length of the slab–weak-layer system, which governs stress redistribution within the slab and the transfer of load to the weak layer,

$$\Lambda = \sqrt{\frac{E'h u_p}{\tau_p}}. \quad (7)$$

This is the same characteristic length appearing in the weak-spot model of Gaume et al. [2013]. The second is the length associated with finite softening, or fracture process zone length,

$$\ell = \sqrt{\frac{E'h \delta}{\tau_p - \tau_r}}. \quad (8)$$

#### 3.2 Closed-form solution

##### 3.2.1 Critical lengths

Solving the system's governing Eq. (2) in the residual, softening and intact regions, and enforcing continuity of displacement and displacement gradient at  $x = a_c$  and  $x = b_c$ , gives a scalar equation for the dimensionless softening zone length

$$\alpha = \frac{b_c - a_c}{\ell}. \quad (9)$$

This equation is

$$(\tau_g - \tau_r) + (\tau_p - \tau_g) \cos \alpha = (\tau_p - \tau_g) \frac{\Lambda}{\ell} \sin \alpha. \quad (10)$$

Equivalently,

$$\alpha = \arccos \left( -\frac{\tau_g - \tau_r}{(\tau_p - \tau_g) \sqrt{1 + (\Lambda/\ell)^2}} \right) - \arctan \left( \frac{\Lambda}{\ell} \right). \quad (11)$$

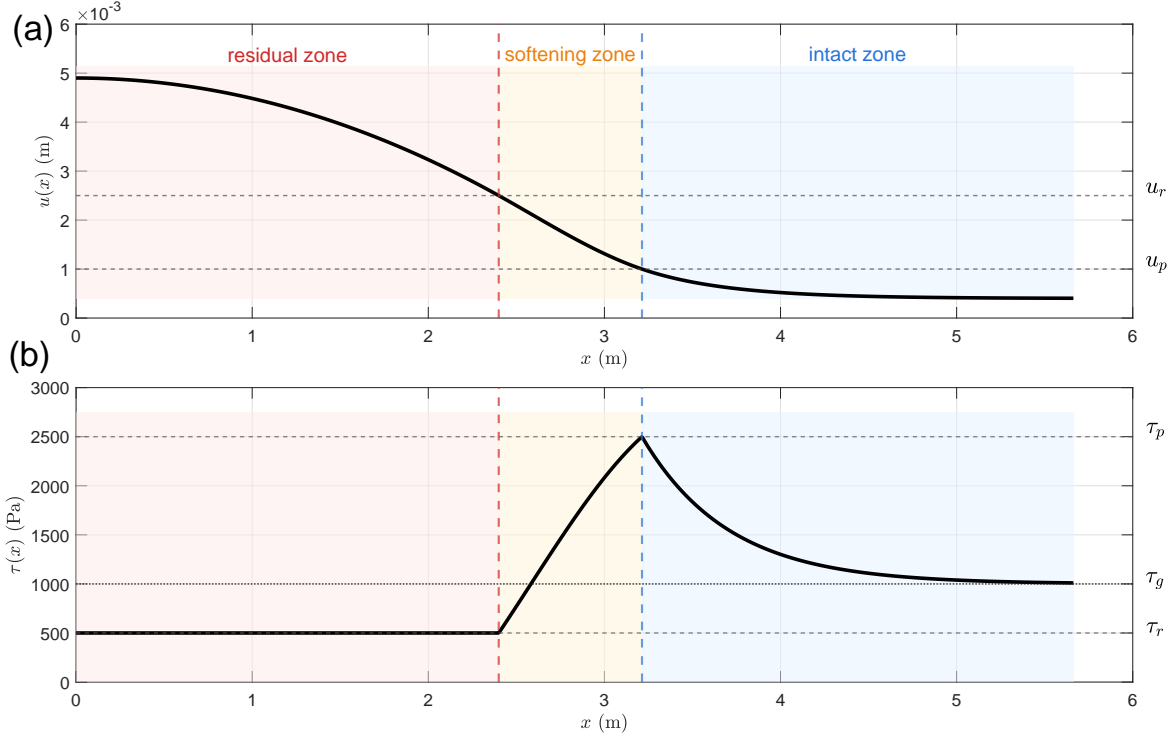


Figure 3: Solution for the tangential displacement  $u(x)$  and shear stress  $\tau(x)$  in the three regions for a specific set of parameters.

The fully residual half-length is then

$$a_c = \ell \frac{\frac{\tau_p - \tau_g}{\tau_g - \tau_r} + \cos \alpha}{\sin \alpha}, \quad (12)$$

and the total affected half-length is

$$b_c = a_c + \ell \alpha. \quad (13)$$

For consistency, we use the following terminology throughout. We denote by  $a_c$  the critical crack length, corresponding to the fully softened region where the weak layer has reached residual strength. The quantity  $b_c$  includes both this crack and the softening zone, where the weak layer is partially softened but has not yet reached residual strength. We therefore refer to  $b_c$  as the critical propagation length. Finally, the fracture process zone length, is defined as

$$\omega = \ell \alpha = b_c - a_c.$$

Figure 2 shows the evolution of the critical crack length  $a_c$ , the critical affected-zone length  $b_c$ , and the softening length  $\omega$ , all normalized by the brittle critical length  $a_{c0}$ , as functions of the softening distance  $\delta$ .

### 3.2.2 Tangential displacement and shear stress profiles

The corresponding displacement and stress fields at the critical state are obtained in compact form as follows. In the residual zone,  $0 \leq x \leq a_c$ , the stress is constant,  $\tau_I(x) = \tau_r$ , and the displacement is parabolic:

$$u_I(x) = u_0 + \frac{\tau_r - \tau_g}{2E'h} x^2, \quad (14)$$

where  $u_0$  is fixed by the condition  $u_I(a_c) = u_r = u_p + \delta$ . In the softening zone,  $a_c \leq x \leq b_c$ , the displacement takes the form

$$u_{II}(x) = u_c + A \cos\left(\frac{x - a_c}{\ell}\right) + B \sin\left(\frac{x - a_c}{\ell}\right), \quad (15)$$

with

$$u_c = u_p + \delta \frac{\tau_p - \tau_g}{\tau_p - \tau_r}, \quad A = \delta \frac{\tau_g - \tau_r}{\tau_p - \tau_r}, \quad B = -A \frac{a_c}{\ell},$$

and the stress follows directly from the softening law,

$$\tau_{II}(x) = \tau_p - \frac{\tau_p - \tau_r}{\delta} (u_{II}(x) - u_p). \quad (16)$$

Finally, in the intact zone,  $x \geq b_c$ , the bounded solution is exponential,

$$u_{III}(x) = \frac{\tau_g}{\tau_p} u_p + u_p \frac{\tau_p - \tau_g}{\tau_p} e^{-(x - b_c)/\Lambda}, \quad (17)$$

and the stress is given by the elastic branch,

$$\tau_{III}(x) = \frac{\tau_p}{u_p} u_{III}(x). \quad (18)$$

These expressions provide the full displacement and stress profiles associated with the critical state. The detailed derivation of Eqs. (10)–(13) is given in Appendix A.

### 3.3 Brittle limit

In the brittle limit  $\delta \rightarrow 0$ , the fracture process zone length  $\ell$  tends to zero while  $\Lambda$  remains finite. Hence  $\Lambda/\ell \rightarrow \infty$ . Equation (10) then requires  $\alpha \rightarrow 0$ , so that the process zone length  $\omega = \ell\alpha$  also vanishes. The residual-zone length and the total affected length therefore become identical.

Expanding Eq. (10) for small  $\alpha$  gives

$$\alpha \sim \frac{\tau_p - \tau_r}{\tau_p - \tau_g} \frac{\ell}{\Lambda}. \quad (19)$$

Substitution into Eq. (12) gives

$$a_c \rightarrow a_{c0} = \Lambda \frac{\tau_p - \tau_g}{\tau_p - \tau_r}. \quad (20)$$

Since  $\omega \rightarrow 0$ , the total affected length satisfies

$$b_c \rightarrow a_{c0}. \quad (21)$$

Thus, the present fracture-process-zone solution recovers the classical stress-based weak-spot result in the limit of vanishing softening displacement [Gaume et al., 2013].

## 4 Small-softening approximation $\delta \rightarrow 0$

Although the exact solution presented above is already compact, recent numerical work by Meloche et al. [2025], based on a depth-averaged MPM formulation using the same constitutive framework presented here (weak layer interface model and slab elasticity), suggested that the influence of  $\delta$  on the critical length could be captured by a square-root correction of the form  $\sqrt{1 + C\delta/u_p}$ . This motivated us to expand the exact solution for small softening displacement. The details of the expansion are given in Appendix B; here we only report the resulting compact expressions.

For small but finite softening displacement, the exact solution admits the asymptotic approximation

$$a_c = a_{c0} \sqrt{1 + C_a \frac{\delta}{u_p}} + O\left[\left(\frac{\delta}{u_p}\right)^3\right], \quad (22)$$

with

$$C_a = \frac{\tau_p(\tau_p - 2\tau_g + \tau_r)}{(\tau_p - \tau_g)^2}. \quad (23)$$

This expression is asymptotically consistent with the exact solution up to and including terms of order  $(\delta/u_p)^2$ . It also satisfies the brittle limit explicitly,

$$a_c \rightarrow a_{c0} \quad \text{as} \quad \delta \rightarrow 0.$$

The corresponding fracture-process-zone length follows from  $\omega = \ell\alpha$ . Using the brittle-limit expansion of  $\alpha$ , one obtains the leading-order approximation

$$\omega \simeq \Lambda \frac{\tau_p}{\tau_p - \tau_g} \frac{\delta}{u_p}. \quad (24)$$

Thus, although the intrinsic softening length  $\ell$  scales as  $\delta^{1/2}$ , the actual process-zone length  $\omega = b_c - a_c$  grows linearly with the softening displacement in the small- $\delta$  regime.

The total affected length then follows as

$$b_c \simeq a_c + \omega. \quad (25)$$

If expanded to first order in  $\delta/u_p$ , this is equivalent to

$$b_c \simeq a_{c0} \sqrt{1 + C_b \frac{\delta}{u_p}}, \quad (26)$$

where

$$C_b = \frac{\tau_p(\tau_p - \tau_r)}{(\tau_p - \tau_g)^2}. \quad (27)$$

Unlike  $C_a$ , the coefficient  $C_b$  is positive for  $\tau_p > \tau_r$ . Therefore, the total affected length  $b_c$  always increases with softening displacement in the small- $\delta$  regime, whereas the fully residual length  $a_c$  increases only if  $\tau_g < (\tau_p + \tau_r)/2$ . This distinction is important when comparing the analytical solution to numerical simulations. If the numerical model measures the full damaged or affected region, including the process zone, then  $b_c$ , rather than  $a_c$ , is the appropriate analytical quantity for comparison.

## 5 Model verification

Simulations based on the depth-averaged Material Point Method (DAMPM) were performed using the same shear softening law as that assumed in the analytical model. The main difference lies in the boundary condition at  $x = 0$ : instead of imposing symmetry in the numerical setup, we explicitly simulated a centered weak spot. In addition, the DAMPM simulations are not strictly quasi-static. Even for very slow cutting, a small slab acceleration develops within the residual zone. To account for this effect, we introduced a local inertial correction term  $\rho h \ddot{u}_{\text{res}}$  on the right-hand side of Eq. (2) and only in the residual region, with  $\ddot{u}_{\text{res}}$  determined in DAMPM. Hence, the correction modifies only the residual-zone curvature and the value of  $u(0)$ , while leaving the matching at  $x = a_c$ , and therefore the analytical values of  $a_c$  and  $b_c$ , unchanged.

Overall, the agreement between analytical and numerical results is very good (Fig. 4). In particular, the tangential displacement and shear stress profiles compare well (Figs. 4a and 4b), and the analytical model accurately reproduces the dependence of the critical crack length  $a_c$ , the total affected critical length  $b_c$ , and the fracture-process-zone length  $\omega = b_c - a_c$  on the softening displacement (Fig. 4c).

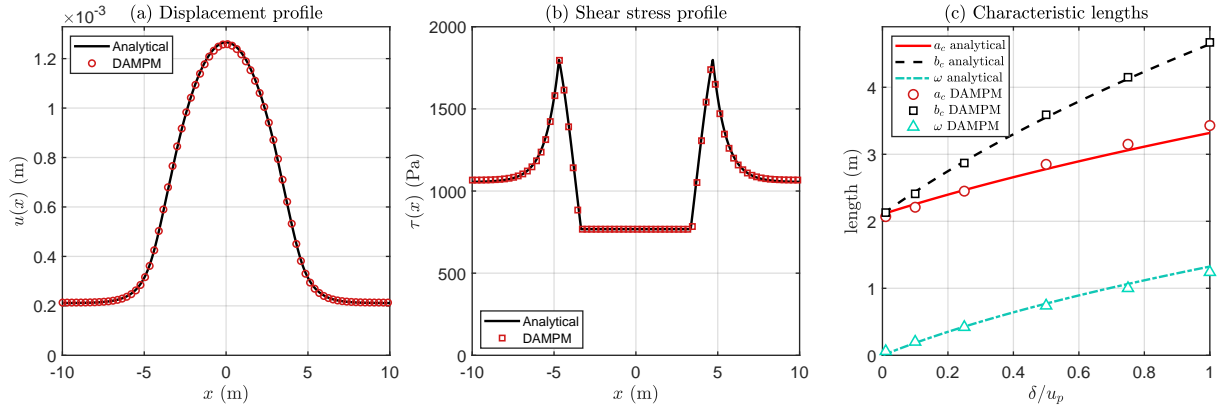


Figure 4: Comparison between the analytical slab–weak-layer softening solution and DAMPM results. (a) Tangential displacement profile  $u(x)$  for  $\delta/u_p = 1$ . (b) Corresponding shear stress profile  $\tau(x)$ . (c) Critical crack length  $a_c$ , critical affected length  $b_c$ , and length of the fracture process zone  $\omega$  as a function of the normalized softening displacement  $\delta/u_p$ . Analytical predictions are shown by black lines and DAMPM results by red symbols. In panels (a) and (b), the analytical solution includes a local residual-zone dynamic correction to improve comparison with the non-quasi-static DAMPM profiles, while the critical lengths in panel (c) correspond to the original quasi-static analytical solution. For readability, the DAMPM profiles in panels (a) and (b) are shown using subsampled markers; these symbols do not represent the actual numerical grid points. The simulations were performed with a spatial resolution of 2 cm, for which plotting every point would make the markers overlap and obscure the comparison.

## 6 Discussion

### 6.1 Physical interpretation

The present solution provides a bridge between two limiting descriptions of weak-layer shear failure. In the brittle limit  $\delta \rightarrow 0$ , the weak layer drops abruptly from peak to residual strength and the formulation reduces to the stress-based weak-spot criterion of Gaume et al. [2013]. For finite  $\delta$ , a softening zone develops ahead of the fully residual region, thereby introducing into the weak-spot framework the strain-softening picture originally emphasized by McClung [1979]. In this sense, the model extends the brittle stress-based approach to finite softening without the need to impose an additional fracture criterion externally: fracture-energy effects enter naturally through the constitutive law and the resulting emergence of a softening zone often referred to as fracture process zone in the literature. In the limiting case  $u_p = 0$ , the weak layer becomes non-compliant prior to peak failure, so that the elastic characteristic length associated with pre-peak stress redistribution disappears. The problem is then governed entirely by post-peak softening and by the associated fracture-process-zone length. This limiting case should therefore not be viewed as recovering exactly the formulation of McClung [1979], but rather as recovering the same class of post-peak shear-propagation models. In this respect, the present framework is also close in spirit to the process-zone and energy-balance approaches of Puzrin and Germanovich [2005], although the result is obtained here directly from an exact slab–weak-layer constitutive solution.

A central result is that two crack-length measures must be distinguished. The length  $a_c$  denotes only the portion of the weak layer that has already reached residual strength, whereas  $b_c$  denotes the total affected length, including both the residual region and the softening zone. These two quantities should therefore not be used interchangeably. This distinction is particularly important when comparing the analytical solution with numerical simulations or observations, because the measured crack length may correspond to the full damaged region rather than

to the fully residual part alone. In the present model,  $b_c$  always increases with  $\delta$  for  $\tau_p > \tau_r$ , reflecting the finite width of the softening zone. By contrast, the first-order correction to  $a_c$  is governed by

$$C_a = \frac{\tau_p(\tau_p - 2\tau_g + \tau_r)}{(\tau_p - \tau_g)^2},$$

which changes sign when  $\tau_g = (\tau_p + \tau_r)/2$ . Accordingly, if  $\tau_g < (\tau_p + \tau_r)/2$ , finite softening increases the fully residual critical length, whereas if  $\tau_g > (\tau_p + \tau_r)/2$ , it decreases it.

This latter result may appear counterintuitive, since introducing softening also introduces a fracture-energy-like dissipation, and one might therefore expect the critical crack length to increase systematically. The solution shows that this intuition applies more directly to the total affected length  $b_c$ , not necessarily to the fully residual length  $a_c$ . Indeed,  $a_c$  measures only the part of the weak layer that has already reached residual strength, while the softening zone ahead of it already contributes to stress redistribution and weakening. As a result, when the gravitational shear stress is sufficiently close to the peak strength, the system may become unstable with a shorter fully residual core because part of the required weakening is already provided by the softening zone. This does not mean that fracture energy promotes failure in an energetic sense; rather, it means that the relevant measure of the destabilized region is no longer  $a_c$  alone. The physically more complete quantity is  $b_c = a_c + \ell\alpha$ , which accounts for the full region involved in the failure process.

The model remains deliberately idealized: it is one-dimensional, static, and based on a local shear stress–displacement law. Nevertheless, it provides a compact analytical benchmark for numerical models and clarifies how finite softening modifies the critical conditions for shear-failure propagation, while also showing that the interpretation of “critical crack length” depends on whether one refers to the fully residual region or to the total affected zone.

## 6.2 Connection to fracture energy

For the linear softening law adopted here, the mode II fracture energy of the weak layer is

$$G_{IIc} = \int_{u_p}^{u_r} (\tau(u) - \tau_r) du = \frac{1}{2}(\tau_p - \tau_r)\delta. \quad (28)$$

Therefore,

$$\delta = \frac{2G_{IIc}}{\tau_p - \tau_r}. \quad (29)$$

The softening length can then be written as

$$\ell = \frac{\sqrt{2E'hG_{IIc}}}{\tau_p - \tau_r}. \quad (30)$$

Thus, the brittle stress-based solution is recovered in the limit  $G_{IIc} \rightarrow 0$ , while finite fracture energy introduces a finite process zone and modifies both  $a_c$  and  $b_c$ .

Furthermore, note that although the comparison presented in Appendix B of Gaume et al. [2014] is mathematically correct within its own assumptions, it is not fully consistent with the more complete shear-softening framework developed here. In particular, that appendix compares, in energetic terms, a purely brittle stress-based formulation with a fracture-type approach that neglects weak-layer pre-peak compliance. The present analysis clarifies that a general shear-softening description should explicitly distinguish between pre-peak compliance and post-peak softening, thereby introducing two characteristic lengths. The earlier interpretation should therefore be viewed as applying to two reduced end-member formulations rather than to the fully general shear-softening problem.

### 6.3 Extension to anticrack propagation

Although the present derivation was restricted to slope-parallel shear failure, the same idea can be extended to mixed-mode anticrack propagation, where weak-layer collapse and slab bending play a central role. Inspired by the beam-on-elastic-foundation framework of Rosendahl and Weissgraeber [2020a,b], Weissgraeber and Rosendahl [2023], we consider a simplified flat anticrack analogue in which the slab is described by an Euler–Bernoulli bending model and the weak layer by a one-dimensional compressive support law. This deliberately neglects Timoshenko shear deformation of the slab in order to retain a compact three-zone analytical structure. A Timoshenko version could in principle be solved with the same matching strategy, since the governing equations remain linear with constant coefficients in each zone, but the characteristic roots would involve both bending and shear-deformation length scales, making the derivation considerably more cumbersome. In its simplest flat form, the bending-dominated problem is governed by

$$\mathcal{B}w'''' + \sigma(w) = \sigma_g,$$

where  $w$  is the slope-normal slab deflection,  $\mathcal{B}$  is the slab bending stiffness,  $\sigma_g$  is the normal slab load, and  $\sigma(w)$  is the compressive weak-layer support.

In the brittle limit, the intact slab satisfies

$$\mathcal{B}w'''' + k_n w = \sigma_g.$$

The bounded solution ahead of the collapsed zone decays over the bending-foundation length

$$\Lambda_b = \left( \frac{4\mathcal{B}}{k_n} \right)^{1/4}.$$

Matching this intact solution to a one-sided collapsed region gives the brittle flat anticrack length

$$a_{c0} = \Lambda_b \left[ \sqrt{1 + \frac{\sigma_p - \sigma_g}{\sigma_g - \sigma_r}} - 1 \right],$$

or, for negligible residual support  $\sigma_r = 0$ ,

$$a_{c0} = \Lambda_b \left( \sqrt{\frac{\sigma_p}{\sigma_g}} - 1 \right).$$

This expression is reminiscent of the bending-related correction proposed by Gaume et al. [2017] on the basis of DEM simulations.

For a finite compressive softening distance  $\delta$ , the tangent stiffness of the softening branch is

$$k_s = \frac{\sigma_p - \sigma_r}{\delta}.$$

Balancing bending with this softening stiffness introduces the bending-softening length

$$\ell_b = \left( \frac{\mathcal{B}}{k_s} \right)^{1/4} = \left( \frac{\mathcal{B}\delta}{\sigma_p - \sigma_r} \right)^{1/4}.$$

This fourth-root dependence differs from the shear-only problem, where the softening length scales as

$$\ell \sim \left( \frac{E'h\delta}{\tau_p - \tau_r} \right)^{1/2}.$$

The difference reflects the order of the governing operator: mixed-mode collapse is controlled by a fourth-order bending equation, whereas the shear-band problem is controlled by a second-order axial equilibrium equation.

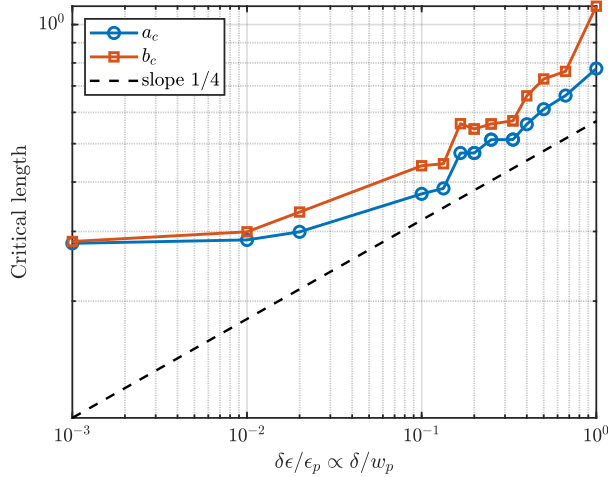


Figure 5: Effect of the normalized compressive softening distance on the characteristic anticrack lengths obtained from 3D MPM simulations based on the model of Gaume et al. [2018]. The collapsed length  $a_c$  and the total affected length  $b_c$  are plotted as functions of  $\Delta\epsilon/\epsilon_p \simeq \delta/w_p$  in log–log scale. Both lengths exhibit an approximately quarter-power dependence over the explored range, consistent with the bending-softening length  $\ell_b \sim (\mathcal{B}\delta/(\sigma_p - \sigma_r))^{1/4}$  predicted by the flat compressive anticrack analogue. The dashed line indicates a reference slope of 1/4.

The finite-softening compressive anticrack problem can be solved exactly by a three-zone construction composed of a residual collapsed zone, a linear softening zone and an intact elastic zone. As shown in Appendix C, the full fourth-order boundary-value problem reduces to three nonlinear matching equations for the collapsed length, the softening-zone length and the residual-zone rotation. Thus, the solution contains both the brittle bending-foundation length  $\Lambda_b$  and the softening length  $\ell_b$ .

The MPM simulations suggest that, over the explored range of  $\delta/w_p$ , both the collapsed length  $a_c$  and the total affected length  $b_c$  exhibit an apparent quarter-power dependence on the compressive softening distance, while consistently approaching the brittle limit  $a_c = b_c = a_{c0}$  as  $\delta \rightarrow 0$ . Guided by the exact three-zone reduction and supported by the MPM scaling, a compact global approximation preserving the brittle limit is

$$a_c(\delta) \simeq a_{c0} \left( 1 + C_a^{(b)} \frac{\delta}{w_p} \right)^{1/4}, \quad b_c(\delta) \simeq a_{c0} \left( 1 + C_b^{(b)} \frac{\delta}{w_p} \right)^{1/4},$$

where  $C_a^{(b)}$  and  $C_b^{(b)}$  are dimensionless coefficients determined by the full matching problem and by the compressive collapse law. This form satisfies

$$a_c(0) = b_c(0) = a_{c0},$$

while recovering an apparent  $\delta^{1/4}$ -scaling when the finite-softening term dominates.

The fourth-root exponent should therefore be interpreted as a signature of the bending-controlled process-zone scale, not as evidence that the finite-softening effect is necessarily small. The actual magnitude of the change in  $a_c$  or  $b_c$  over a finite range of  $\delta/w_p$  also depends on the prefactors  $C_a^{(b)}$  and  $C_b^{(b)}$ , and can therefore be substantial. In a more complete Timoshenko beam formulation, slab shear deformation would introduce an additional softening length so that finite softening could in principle enter through both  $\delta^{1/4}$ - and  $\delta^{1/2}$ -type scales. However, the MPM results shown in Fig. 5 exhibit a quarter-power trend over the explored range, suggesting that the bending-controlled contribution dominates for the configurations considered here. This scaling

nevertheless provides a useful contrast with the slope-parallel shear case and offers a mechanistic perspective on why strength and toughness may enter differently in collapse-dominated mixed-mode propagation [Rosendahl and Weissgraeber, 2020a,b].

#### 6.4 Bending-induced shear and mixed-mode correction

The flat compressive anticrack analogue was formulated with a normal foundation only. However, slab bending also induces basal rotation. If the weak layer resists the associated tangential displacement, this rotation generates an additional shear stress. For consistency with the anticrack interpretation, we consider the collapsed region as unsupported in both normal and tangential directions. Thus, in this mixed-mode extension,

$$\sigma_r = 0, \quad \tau_r = 0.$$

This avoids introducing residual normal or frictional shear resistance inside a void-like collapsed zone.

Using Euler–Bernoulli kinematics, the basal tangential displacement induced by bending is of order

$$u_{\text{bend}} \simeq \frac{h}{2} w'(b_c),$$

where  $b_c$  is the leading edge of the affected zone. With the pre-peak tangential stiffness  $k_t = \tau_p/u_p$ , the corresponding shear stress is

$$\tau_{\text{bend}} \simeq \frac{\tau_p}{u_p} \frac{h}{2} w'(b_c),$$

or

$$\frac{\tau_{\text{bend}}}{\tau_p} \simeq \frac{h}{2u_p} w'(b_c).$$

For the finite-softening anticrack solution, the rotation  $w'(b_c)$  is obtained by solving the three-zone bending problem composed of a collapsed zone, a linear softening zone and an intact elastic zone. In the softening zone, the deflection is written as a linear combination of hyperbolic and trigonometric functions. Evaluating this solution and its derivatives at the leading edge  $x = b_c$  introduces the matching quantities  $S_1$  and  $S_2$ , defined such that

$$w'(b_c) = \frac{S_1}{\ell_b}, \quad w''(b_c) = \frac{S_2}{\ell_b^2}.$$

Their full expressions in terms of the softening-zone coefficients are given in Appendix C and Appendix D. Here,  $S_1$  represents the dimensionless rotation-like matching quantity, while  $S_2$  represents the corresponding curvature-like matching quantity. The bending-softening length is

$$\ell_b = \left( \frac{\mathcal{B}\delta}{\sigma_p} \right)^{1/4},$$

for the void-like case  $\sigma_r = 0$ . Using the rotation matching condition at  $x = b_c$ , one obtains

$$\frac{S_1}{\ell_b} = -\frac{\sigma_p - \sigma_g}{k_n \Lambda_b} - \frac{\Lambda_b}{2} \frac{S_2}{\ell_b^2},$$

with

$$\Lambda_b = \left( \frac{4\mathcal{B}}{k_n} \right)^{1/4}.$$

Therefore,

$$\frac{\tau_{\text{bend}}}{\tau_p} \simeq -\frac{h}{2u_p} \left[ \frac{\sigma_p - \sigma_g}{k_n \Lambda_b} + \frac{\Lambda_b}{2} \frac{S_2}{\ell_b^2} \right].$$

This expression displays explicitly two contributions: the first term is controlled by the intact bending-foundation length  $\Lambda_b$ , while the second term contains the finite-softening correction through the ratio  $\Lambda_b/\ell_b^2$  and the curvature-like matching quantity  $S_2$ .

In the brittle limit, the softening zone collapses,  $b_c \rightarrow a_c$ , and the rotation reduces to the brittle flat anticrack value

$$w'_0 = -\frac{2w_p}{\Lambda_b} \left( 1 - \sqrt{\frac{\sigma_g}{\sigma_p}} \right),$$

so that

$$\frac{|\tau_{\text{bend}}^{(0)}|}{\tau_p} \simeq \frac{h}{\Lambda_b} \frac{w_p}{u_p} \left( 1 - \sqrt{\frac{\sigma_g}{\sigma_p}} \right).$$

Thus, the leading-order brittle contribution is governed by the dimensionless factor

$$\frac{h}{\Lambda_b} \frac{w_p}{u_p},$$

whereas finite compressive softening modifies this estimate through the additional process-zone term involving  $S_2/\ell_b^2$ . Equivalently, one may write

$$w'(b_c) = w'_0 + \Delta w'_\delta, \quad \Delta w'_\delta = \frac{S_1}{\ell_b} - w'_0,$$

so that

$$\frac{\tau_{\text{bend}}}{\tau_p} \simeq \frac{h}{2u_p} (w'_0 + \Delta w'_\delta).$$

The correction  $\Delta w'_\delta$  should not be treated as an independent physical stress contribution: it is simply the change in slab rotation produced by the finite softening zone in the full three-zone solution.

The shear stress entering a reduced mixed-mode criterion can then be estimated as

$$\tau_{\text{tip}} = \tau_g \left( 1 + \frac{b_c}{\Lambda} \right) + \tau_{\text{bend}},$$

where

$$\Lambda = \sqrt{\frac{E' h u_p}{\tau_p}}$$

is the shear stress-transfer length. This form is consistent with the flat limit: if  $\tau_g = 0$ , the shear-transfer contribution vanishes and the only remaining shear component is the one induced by slab bending.

The normal stress at the leading edge of the affected zone may be estimated from the bending-foundation amplification. In the brittle limit,

$$\sigma_{\text{tip}} \simeq \sigma_g \left( 1 + \frac{b_c}{\Lambda_b} \right)^2.$$

Finite compressive softening introduces the bending-softening length  $\ell_b$ . Thus, the reduced finite-softening correction can be interpreted as replacing the brittle bending length  $\Lambda_b$  by an effective bending length controlled by both  $\Lambda_b$  and  $\ell_b$ . A compact representation, consistent with the observed quarter-power scaling, is

$$\Lambda_{b,\text{eff}} = \Lambda_b \left( 1 + C_b^{(b)} \frac{\delta}{w_p} \right)^{1/4},$$

so that

$$\sigma_{\text{tip}} \simeq \sigma_g \left( 1 + \frac{b_c}{\Lambda_{b,\text{eff}}} \right)^2.$$

Equivalently, this effective length can be viewed as a reduced way of representing the finite process-zone correction associated with the ratio  $\ell_b/\Lambda_b$ . In the full formulation of Appendix D, however,  $\sigma_{\text{tip}}$  is not prescribed by this approximation but is solved directly as part of the four-equation matching problem.

The onset of local softening at the leading edge of the affected zone is then described by a mixed-mode peak surface, for example

$$\left(\frac{\tau_{\text{tip}}}{\tau_p}\right)^2 + \left(\frac{\sigma_{\text{tip}}}{\sigma_p}\right)^2 = 1.$$

In the pure compressive limit,  $\tau_{\text{tip}} = 0$  and  $\sigma_{\text{tip}} = \sigma_p$ . In mixed mode, neither component needs to reach its pure-mode peak value independently. This provides a simple way to account for the shear generated both by slope-parallel loading and by slab bending, while retaining the bending-controlled length scales  $\Lambda_b$  and  $\ell_b$  of the anticrack solution. The full finite-softening mixed-mode matching problem is given in Appendix D.

## 6.5 Experimental constraints on the softening displacement

Stress–deformation measurements of weak snow layers remain scarce. McClung [1979] reported a shear stress–tangential displacement curve for a thin dry snow sample, showing pronounced post-peak softening and introducing the concept of a finite softening distance  $\delta$ . However, the experiments published in McClung [1979] and described in details McClung [1977] were performed at very low strain rates, below  $10^{-4} \text{ s}^{-1}$ , which is not representative of the nearly brittle response expected during artificial avalanche triggering or in classical snow-fracture tests. These experiments, and the conclusions drawn from them, are therefore likely more relevant to natural avalanche release, for which the ductile-to-brittle transition of snow may play an important role [Puzrin et al., 2019]. More recently, Schöttner et al. [2025] presented stress–strain curves for depth-hoar weak layers that also exhibit pronounced softening after peak failure with a finite and non-negligible softening length. Yet, the measured strain rates measured by digital image correlation were of the order of  $10^{-3} \text{ s}^{-1}$ , such that ductile effects cannot be ruled out [Puzrin et al., 2019].

At higher loading rates, one may instead expect an even sharper, more brittle-like response. This interpretation is supported by the experimental results of Schweizer [1998] and by displacement-controlled tests reported in Ingrid Reiweger’s thesis [Reiweger, 2011]. In particular, the tested BB samples display a very abrupt post-peak stress drop, suggesting values of  $\delta$  that are significantly smaller than the peak displacement  $u_p$ , as illustrated in Fig. 6. Reiweger’s experiments suggest a maximum ratio  $\delta/u_p \approx 0.1$ . This value should, however, be regarded as an upper bound, since it is essentially limited by the acquisition frequency: no data point is available within the softening branch itself, and the measurements only capture a direct drop from peak to residual stress. In practice, the true value of  $\delta$  may therefore be smaller.

Within the present shear-based weak-layer interface framework, even the upper-bound value  $\delta/u_p \approx 0.1$  would lead to a limited increase in the critical propagation length, of the order of 10% at most for the parameters considered here. This suggests that, for supershear crack propagation driven primarily by weak-layer shear failure, a purely stress-strength-based criterion may be sufficient as a first approximation.

The situation may be different for mixed-mode anticrack nucleation, where weak-layer collapse and slab bending are central. Both the simplified compressive anticrack analogue developed above and preliminary 3D MPM simulations suggest that the contribution of finite softening can be larger in this regime. In particular, the MPM results indicate an increase of about 40% in the critical crack length for  $\delta/w_p \approx 0.1$ . This result should nevertheless be interpreted with care. In an interface model, failure is necessarily localized across the entire weak layer, whereas in a finite-thickness weak layer the deformation may localize only within a portion of the layer. This

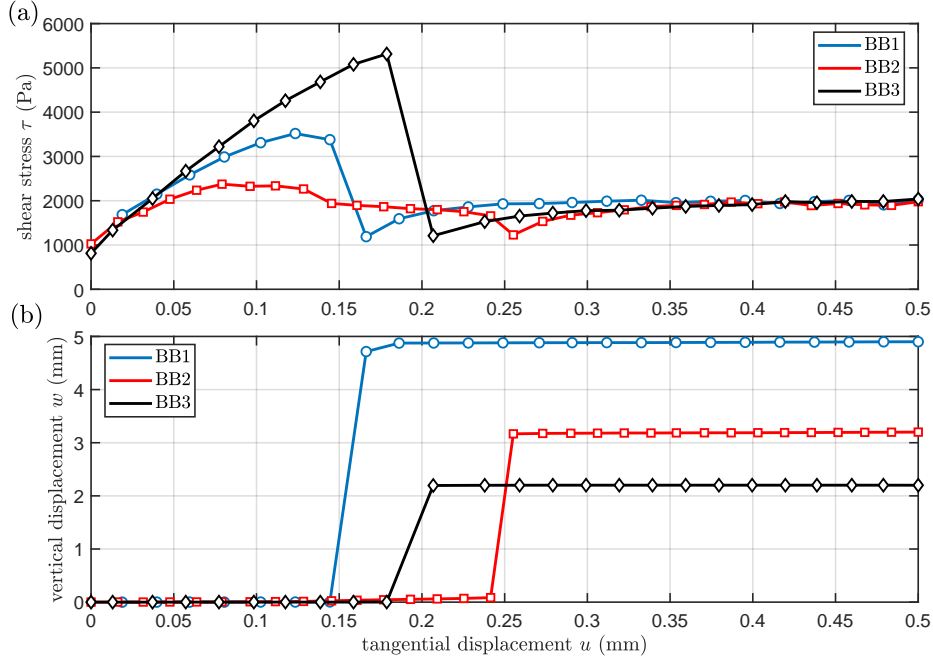


Figure 6: Displacement-controlled direct shear experiments on BB snow samples from the thesis of Ingrid Reiweger. (a) Shear stress versus tangential displacement. (b) Corresponding vertical displacement versus tangential displacement. The experiments were performed with the low-temperature fracture tester at a laboratory temperature of  $-6^\circ\text{C}$ , under an applied normal stress of  $\sigma_z = 0.9 \pm 0.3$  kPa. The imposed displacement rate was constant during each test, so that the reported curves represent displacement-controlled shear loading. The measured strain rate using DIC was found around  $0.012 \text{ s}^{-1}$ .

makes the effective interpretation of  $\delta$  and  $w_p$  less direct, especially because the present MPM model is not yet regularized.

Overall, these considerations suggest that the brittle critical length remains dominant for shear-driven supershear propagation, whereas both the brittle length and the finite softening zone may be important for the onset of mixed-mode anticrack propagation. In the latter case, finite softening introduces a distinct bending-controlled  $\delta^{1/4}$ -type scale rather than the  $\delta^{1/2}$ -type shear scale. This difference in exponent should not be interpreted alone as a statement about the magnitude of the effect, which also depends on prefactors, localization, and the explored range of  $\delta/w_p$ .

## 7 Conclusion

We derived an analytical model of snow slab avalanche release in which crack propagation is governed by shear failure in a weak layer beneath an elastic snow slab, explicitly accounting for both weak-layer pre-peak compliance and finite post-peak softening. The model recovers the classical stress-based critical crack length in the brittle limit and provides closed-form expressions for the fully softened crack length  $a_c$  and for the total affected length  $b_c$ , which also includes the fracture process zone. Our results highlight the need for caution when extracting critical lengths from numerical simulations: the critical crack length associated with the fully softened or residual core should be clearly distinguished from the total length of the affected region, which may include partially damaged or pre-softened material. For small softening displacement, the exact solution admits a compact square-root approximation for the fully softened crack length  $a_c$ ,

while the fracture-process-zone length  $\omega$  grows linearly with the ratio  $\delta/u_p$ . The total affected length  $b_c$  then follows naturally as the sum of these two contributions. Our exact solution rationalizes recent numerical observations and provides a simple correction to the brittle weak-spot solution. The framework also establishes a direct connection between stress-based and fracture-energy-based descriptions through the constitutive softening law itself. Finally, the mixed-mode anticrack analogue introduces a bending-controlled  $\delta^{1/4}$ -type scale, distinct from the  $\delta^{1/2}$ -type shear scale. The magnitude of this effect, however, depends on prefactors and may be substantial over finite parameter ranges. Overall, the present work revisits classical shear-based avalanche-release theory in a more complete mechanical framework, at a time when its relevance has re-emerged through the recent discovery of supershear failure in snow slab avalanches, and provides a compact analytical basis for comparison with experiments and numerical models.

## Acknowledgements

The authors gratefully acknowledge the researchers involved in the discussion of the paper entitled “Parameterization of the snow fracture energy to model the onset of crack propagation in snowpack models” in *The Cryosphere Discussions*, whose comments and exchanges motivated the present work. The authors acknowledge the use of artificial intelligence as a limited exploratory tool during the asymptotic analysis. Motivated by the DAMPM results, which suggested that the effect of finite softening could be represented by a square-root correction, AI was consulted to assess whether such a compact reformulation was algebraically plausible before carrying out the expansion of the exact solution. This use was restricted to exploring a concise representation of an already closed analytical solution; the square-root approximation is not required for the validity of the model, but provides a useful compact form for interpretation and comparison.

## A Derivation of the exact matching conditions

This appendix gives the details leading to Eqs. (10)–(13). We use the notation  $a_c$  for the fully residual half-length,  $b_c$  for the total affected half-length, and

$$\omega = b_c - a_c, \quad \alpha = \frac{\omega}{\ell}.$$

### A.1 Intact zone

In the intact zone,  $x \geq b_c$ , the interface is elastic:

$$\tau(u) = \frac{\tau_p}{u_p} u.$$

Equation (2) becomes

$$E'h u'' - \frac{\tau_p}{u_p} u = -\tau_g. \quad (31)$$

Using

$$\Lambda = \sqrt{\frac{E'h u_p}{\tau_p}},$$

the bounded solution as  $x \rightarrow +\infty$  is

$$u_{III}(x) = \frac{\tau_g}{\tau_p} u_p + u_p \frac{\tau_p - \tau_g}{\tau_p} e^{-(x-b_c)/\Lambda}. \quad (32)$$

Its derivative at  $x = b_c$  is

$$u'_{III}(b_c) = -\frac{u_p}{\Lambda} \frac{\tau_p - \tau_g}{\tau_p} = -\frac{\Lambda}{E'h} (\tau_p - \tau_g). \quad (33)$$

## A.2 Residual zone

In the residual zone,  $0 \leq x \leq a_c$ , the interface carries the constant residual stress  $\tau_r$ . Equation (2) gives

$$E'h u'' = \tau_r - \tau_g. \quad (34)$$

With the symmetry condition  $u'(0) = 0$ , we obtain

$$u'_I(x) = \frac{\tau_r - \tau_g}{E'h} x. \quad (35)$$

Therefore, at  $x = a_c$ ,

$$u'_I(a_c) = \frac{\tau_r - \tau_g}{E'h} a_c. \quad (36)$$

The displacement condition at the residual-softening boundary is

$$u_I(a_c) = u_r = u_p + \delta. \quad (37)$$

## A.3 Softening zone

In the softening zone,  $a_c \leq x \leq b_c$ , the interface follows

$$\tau(u) = \tau_p - \frac{\tau_p - \tau_r}{\delta} (u - u_p).$$

The governing equation becomes

$$E'h u'' + \frac{\tau_p - \tau_r}{\delta} u = \tau_p + \frac{\tau_p - \tau_r}{\delta} u_p - \tau_g. \quad (38)$$

Using

$$\ell = \sqrt{\frac{E'h \delta}{\tau_p - \tau_r}},$$

the solution can be written as

$$u_{II}(x) = u_c + A \cos\left(\frac{x - a_c}{\ell}\right) + B \sin\left(\frac{x - a_c}{\ell}\right), \quad (39)$$

with

$$u_c = u_p + \delta \frac{\tau_p - \tau_g}{\tau_p - \tau_r}. \quad (40)$$

Continuity of displacement at  $x = a_c$  gives

$$A = \delta \frac{\tau_g - \tau_r}{\tau_p - \tau_r}. \quad (41)$$

Continuity of the derivative at  $x = a_c$ , together with Eq. (36), gives

$$B = -\frac{\delta(\tau_g - \tau_r)}{\tau_p - \tau_r} \frac{a_c}{\ell}. \quad (42)$$

Thus,

$$u_{II}(x) = u_c + \delta \frac{\tau_g - \tau_r}{\tau_p - \tau_r} \cos\left(\frac{x - a_c}{\ell}\right) - \delta \frac{\tau_g - \tau_r}{\tau_p - \tau_r} \frac{a_c}{\ell} \sin\left(\frac{x - a_c}{\ell}\right). \quad (43)$$

#### A.4 Matching at $x = b_c$

At  $x = b_c$ , the displacement reaches the peak value  $u_p$ . Using Eq. (43) and  $\alpha = (b_c - a_c)/\ell$ , the displacement condition gives

$$(\tau_p - \tau_g) + (\tau_g - \tau_r) \cos \alpha - (\tau_g - \tau_r) \frac{a_c}{\ell} \sin \alpha = 0. \quad (44)$$

The derivative condition  $u'_{II}(b_c) = u'_{III}(b_c)$ , using Eq. (33), gives

$$(\tau_g - \tau_r) (\ell \sin \alpha + a_c \cos \alpha) = (\tau_p - \tau_g) \Lambda. \quad (45)$$

Solving Eq. (44) for  $a_c/\ell$  yields

$$\frac{a_c}{\ell} = \frac{\tau_p - \tau_g}{\tau_g - \tau_r} + \cos \alpha. \quad (46)$$

Substitution into Eq. (45) gives

$$(\tau_g - \tau_r) + (\tau_p - \tau_g) \cos \alpha = (\tau_p - \tau_g) \frac{\Lambda}{\ell} \sin \alpha, \quad (47)$$

which is Eq. (10). Equations (12) and (13) then follow directly from Eq. (46) and  $b_c = a_c + \ell\alpha$ .

## B Higher-order small-softening expansion

This appendix derives the small-softening expansion used in the main text. We introduce

$$T = \tau_p - \tau_g, \quad R = \tau_g - \tau_r, \quad s = \frac{\ell}{\Lambda}. \quad (48)$$

Equation (10) becomes

$$R + T \cos \alpha = \frac{T}{s} \sin \alpha. \quad (49)$$

For  $s \ll 1$ , we seek

$$\alpha = ms + ns^3 + ps^5 + O(s^7). \quad (50)$$

Using the Taylor expansions of  $\sin \alpha$  and  $\cos \alpha$ , and matching powers of  $s$  in Eq. (49), one obtains

$$m = \frac{T + R}{T}, \quad n = \frac{m^2(m - 3)}{6}, \quad p = \frac{m^3(8 - 9m + 3m^2)}{40}. \quad (51)$$

### B.1 Expansion of the fully residual length

From Eq. (12),

$$a_c = \Lambda s \frac{T/R + \cos \alpha}{\sin \alpha}. \quad (52)$$

Using Eq. (51), expansion to order  $s^4$  gives

$$a_c = \frac{\Lambda N_0}{m} + \frac{\Lambda}{2} (N_0 - m) s^2 - \frac{\Lambda}{8} m (N_0 - m)^2 s^4 + O(s^6), \quad (53)$$

where

$$N_0 = \frac{T}{R} + 1 = \frac{T + R}{R}. \quad (54)$$

The leading term is

$$a_{c0} = \frac{\Lambda N_0}{m} = \Lambda \frac{T}{R} = \Lambda \frac{\tau_p - \tau_g}{\tau_g - \tau_r}. \quad (55)$$

Moreover,

$$s^2 = \frac{\ell^2}{\Lambda^2} = \frac{\tau_p}{\tau_p - \tau_r} \frac{\delta}{u_p}. \quad (56)$$

Converting Eq. (53) to powers of  $\delta/u_p$  gives

$$a_c = a_{c0} + \tilde{C}_{2,a} \frac{\delta}{u_p} + \tilde{C}_{4,a} \left( \frac{\delta}{u_p} \right)^2 + O \left[ \left( \frac{\delta}{u_p} \right)^3 \right], \quad (57)$$

with

$$\tilde{C}_{2,a} = \frac{\Lambda \tau_p (\tau_p - 2\tau_g + \tau_r)}{2(\tau_g - \tau_r)(\tau_p - \tau_g)}, \quad (58)$$

and

$$\tilde{C}_{4,a} = -\frac{\Lambda \tau_p^2 (\tau_p - 2\tau_g + \tau_r)^2}{8(\tau_p - \tau_g)^3 (\tau_g - \tau_r)}. \quad (59)$$

We now compare this expansion with

$$a_{c0} \sqrt{1 + C_a \frac{\delta}{u_p}} = a_{c0} + \frac{a_{c0} C_a}{2} \frac{\delta}{u_p} - \frac{a_{c0} C_a^2}{8} \left( \frac{\delta}{u_p} \right)^2 + O \left[ \left( \frac{\delta}{u_p} \right)^3 \right]. \quad (60)$$

Matching the coefficient of  $\delta/u_p$  gives

$$C_a = \frac{\tau_p (\tau_p - 2\tau_g + \tau_r)}{(\tau_p - \tau_g)^2}. \quad (61)$$

With this value, the coefficient of  $(\delta/u_p)^2$  is also exactly recovered. Hence,

$$a_c = a_{c0} \sqrt{1 + C_a \frac{\delta}{u_p}} + O \left[ \left( \frac{\delta}{u_p} \right)^3 \right]. \quad (62)$$

## B.2 Expansion of the total affected length

The total affected length is

$$b_c = a_c + \ell \alpha. \quad (63)$$

Since  $\ell = \Lambda s$  and  $\alpha = ms + O(s^3)$ ,

$$\ell \alpha = \Lambda m s^2 + O(s^4). \quad (64)$$

Using Eq. (53), we obtain

$$b_c = a_{c0} + \frac{\Lambda}{2} (N_0 + m) s^2 + O(s^4). \quad (65)$$

Because

$$N_0 + m = \frac{T + R}{R} + \frac{T + R}{T} = \frac{(T + R)^2}{TR}, \quad (66)$$

we obtain

$$b_c = a_{c0} + \frac{\Lambda \tau_p (\tau_p - \tau_r)}{2(\tau_p - \tau_g)(\tau_g - \tau_r)} \frac{\delta}{u_p} + O \left[ \left( \frac{\delta}{u_p} \right)^2 \right]. \quad (67)$$

Matching this first-order expansion with

$$b_c \simeq a_{c0} \sqrt{1 + C_b \frac{\delta}{u_p}}$$

gives

$$C_b = \frac{\tau_p (\tau_p - \tau_r)}{(\tau_p - \tau_g)^2}. \quad (68)$$

## C Anticrack analogue solution on flat terrain

We consider a homogeneous slab on flat terrain, idealized as an Euler–Bernoulli beam with bending stiffness  $\mathcal{B}$ , resting on a weak layer that provides only slope-normal compressive support. The downward slab deflection is denoted by  $w(x)$ , and the normal slab load by  $\sigma_g$ . The weak-layer compressive support law is

$$\sigma(w) = \begin{cases} k_n w, & 0 \leq w \leq w_p, \\ \sigma_p - \frac{\sigma_p - \sigma_r}{\delta} (w - w_p), & w_p \leq w \leq w_r, \\ \sigma_r, & w \geq w_r, \end{cases}$$

with

$$\sigma_p = k_n w_p, \quad w_r = w_p + \delta, \quad \Delta\sigma = \sigma_p - \sigma_r, \quad k_s = \frac{\Delta\sigma}{\delta}.$$

The governing equation is

$$\mathcal{B}w'''' + \sigma(w) = \sigma_g.$$

We introduce three zones: a residual collapsed zone  $0 \leq x \leq a_c$ , a linear softening zone  $a_c \leq x \leq b_c$ , and an intact elastic zone  $x \geq b_c$ . The softening-zone length is

$$\omega = b_c - a_c.$$

### C.1 Residual zone

In the residual zone,  $\sigma = \sigma_r$ , hence

$$\mathcal{B}w_I'''' = \sigma_g - \sigma_r.$$

With free-edge conditions

$$w_I''(0) = 0, \quad w_I'''(0) = 0,$$

the solution is

$$w_I(x) = A_0 + A_1 x + \frac{\sigma_g - \sigma_r}{24\mathcal{B}} x^4.$$

### C.2 Softening zone

In the softening zone,

$$\mathcal{B}w_{II}'''' + \sigma_p - k_s(w_{II} - w_p) = \sigma_g,$$

or

$$\mathcal{B}w_{II}'''' - k_s w_{II} = \sigma_g - \sigma_p - k_s w_p.$$

The bending-softening length is

$$\ell_b = \left(\frac{\mathcal{B}}{k_s}\right)^{1/4} = \left(\frac{\mathcal{B}\delta}{\Delta\sigma}\right)^{1/4}.$$

A constant particular solution is

$$w_c = w_p + \delta \frac{\sigma_p - \sigma_g}{\Delta\sigma}.$$

Thus,

$$w_{II}(x) = w_c + C_1 \cosh\left(\frac{x - a_c}{\ell_b}\right) + C_2 \sinh\left(\frac{x - a_c}{\ell_b}\right) + C_3 \cos\left(\frac{x - a_c}{\ell_b}\right) + C_4 \sin\left(\frac{x - a_c}{\ell_b}\right).$$

### C.3 Intact elastic zone

In the intact region,

$$\mathcal{B}w_{III}'''' + k_n w_{III} = \sigma_g.$$

The bounded solution as  $x \rightarrow +\infty$  relaxes toward  $\sigma_g/k_n$  over the bending-foundation length

$$\Lambda_b = \left( \frac{4\mathcal{B}}{k_n} \right)^{1/4}.$$

It can be written as

$$w_{III}(x) = \frac{\sigma_g}{k_n} + e^{-(x-b_c)/\Lambda_b} \left[ D_1 \cos\left(\frac{x-b_c}{\Lambda_b}\right) + D_2 \sin\left(\frac{x-b_c}{\Lambda_b}\right) \right].$$

### C.4 Matching at $x = a_c$

At  $x = a_c$ , the deflection reaches

$$w_r = w_p + \delta.$$

Continuity of deflection, rotation, curvature and shear gives

$$w_I(a_c) = w_{II}(a_c) = w_r,$$

$$w'_I(a_c) = w'_{II}(a_c), \quad w''_I(a_c) = w''_{II}(a_c), \quad w'''_I(a_c) = w'''_{II}(a_c).$$

This yields

$$C_1 + C_3 = w_r - w_c = \delta \frac{\sigma_g - \sigma_r}{\Delta\sigma},$$

$$C_1 - C_3 = \ell_b^2 \frac{\sigma_g - \sigma_r}{2\mathcal{B}} a_c^2,$$

$$C_2 + C_4 = \ell_b \left( A_1 + \frac{\sigma_g - \sigma_r}{6\mathcal{B}} a_c^3 \right),$$

and

$$C_2 - C_4 = \ell_b^3 \frac{\sigma_g - \sigma_r}{\mathcal{B}} a_c.$$

Therefore,

$$C_1 = \frac{1}{2} \left[ \delta \frac{\sigma_g - \sigma_r}{\Delta\sigma} + \ell_b^2 \frac{\sigma_g - \sigma_r}{2\mathcal{B}} a_c^2 \right],$$

$$C_3 = \frac{1}{2} \left[ \delta \frac{\sigma_g - \sigma_r}{\Delta\sigma} - \ell_b^2 \frac{\sigma_g - \sigma_r}{2\mathcal{B}} a_c^2 \right],$$

$$C_2 = \frac{1}{2} \left[ \ell_b \left( A_1 + \frac{\sigma_g - \sigma_r}{6\mathcal{B}} a_c^3 \right) + \ell_b^3 \frac{\sigma_g - \sigma_r}{\mathcal{B}} a_c \right],$$

and

$$C_4 = \frac{1}{2} \left[ \ell_b \left( A_1 + \frac{\sigma_g - \sigma_r}{6\mathcal{B}} a_c^3 \right) - \ell_b^3 \frac{\sigma_g - \sigma_r}{\mathcal{B}} a_c \right].$$

### C.5 Matching at $x = b_c$

Let

$$\alpha = \frac{b_c - a_c}{\ell_b}.$$

We define

$$S_0 = C_1 \cosh \alpha + C_2 \sinh \alpha + C_3 \cos \alpha + C_4 \sin \alpha,$$

$$S_1 = C_1 \sinh \alpha + C_2 \cosh \alpha - C_3 \sin \alpha + C_4 \cos \alpha,$$

$$S_2 = C_1 \cosh \alpha + C_2 \sinh \alpha - C_3 \cos \alpha - C_4 \sin \alpha,$$

and

$$S_3 = C_1 \sinh \alpha + C_2 \cosh \alpha + C_3 \sin \alpha - C_4 \cos \alpha.$$

Then

$$w_{II}(b_c) = w_c + S_0, \quad w'_{II}(b_c) = \frac{S_1}{\ell_b},$$

$$w''_{II}(b_c) = \frac{S_2}{\ell_b^2}, \quad w'''_{II}(b_c) = \frac{S_3}{\ell_b^3}.$$

At  $x = b_c$ , the deflection reaches the peak value  $w_p$ . Hence,

$$w_{III}(b_c) = w_p,$$

which gives

$$D_1 = w_p - \frac{\sigma_g}{k_n} = \frac{\sigma_p - \sigma_g}{k_n}.$$

For the intact solution,

$$w''_{III}(b_c) = -\frac{2D_2}{\Lambda_b^2}.$$

Curvature continuity therefore gives

$$D_2 = -\frac{\Lambda_b^2}{2} \frac{S_2}{\ell_b^2}.$$

The remaining matching conditions are displacement, rotation and third derivative. They give

$$S_0 + \delta \frac{\sigma_p - \sigma_g}{\Delta \sigma} = 0,$$

$$\frac{S_1}{\ell_b} + \frac{1}{\Lambda_b} \frac{\sigma_p - \sigma_g}{k_n} + \frac{\Lambda_b}{2} \frac{S_2}{\ell_b^2} = 0,$$

and

$$\frac{S_3}{\ell_b^3} - \frac{2}{\Lambda_b^3} \frac{\sigma_p - \sigma_g}{k_n} + \frac{1}{\Lambda_b} \frac{S_2}{\ell_b^2} = 0.$$

The full fourth-order three-zone problem is therefore reduced exactly to three nonlinear matching equations for

$$A_1, \quad a_c, \quad \alpha.$$

Once these are solved,

$$b_c = a_c + \alpha \ell_b.$$

Thus, the displacement field is known analytically in each region, and the only remaining step is the numerical solution of a finite nonlinear matching system.

## C.6 Brittle limit and finite-softening approximation

In the brittle limit  $\delta \rightarrow 0$ , the softening-zone length collapses,

$$\ell_b \rightarrow 0, \quad b_c \rightarrow a_c.$$

The problem then reduces to direct matching between the residual collapsed zone and the intact elastic bending-foundation solution. Keeping a finite residual support  $\sigma_r$ , the brittle length is

$$a_{c0} = \Lambda_b \left[ \sqrt{1 + \frac{\sigma_p - \sigma_g}{\sigma_g - \sigma_r}} - 1 \right].$$

For negligible residual support,  $\sigma_r = 0$ , this becomes

$$a_{c0} = \Lambda_b \left( \sqrt{\frac{\sigma_p}{\sigma_g}} - 1 \right).$$

For finite  $\delta$ , the exact matching system contains the additional bending-softening length

$$\ell_b = \left( \frac{\mathcal{B}\delta}{\sigma_p - \sigma_r} \right)^{1/4}.$$

The finite-softening solution can therefore be viewed as a function of the ratio  $\ell_b/\Lambda_b$ , while satisfying the constraint

$$a_c(0) = b_c(0) = a_{c0}.$$

Guided by the exact three-zone structure and supported by the MPM results, a compact global approximation that preserves this brittle limit is

$$a_c(\delta) \simeq a_{c0} \left( 1 + C_a^{(b)} \frac{\delta}{w_p} \right)^{1/4}, \quad b_c(\delta) \simeq a_{c0} \left( 1 + C_b^{(b)} \frac{\delta}{w_p} \right)^{1/4}.$$

Here  $C_a^{(b)}$  and  $C_b^{(b)}$  are dimensionless coefficients depending on the full matching problem, the residual support and the compressive collapse law. This expression satisfies

$$a_c(0) = b_c(0) = a_{c0},$$

while giving an apparent quarter-power dependence on  $\delta/w_p$  when the finite-softening term dominates. The fourth-root exponent characterizes the bending-controlled process-zone scale, whereas the magnitude of the finite-softening effect over any finite parameter range remains controlled by the prefactors and by the full nonlinear matching problem.

## D Finite-softening mixed-mode anticrack criterion

This appendix extends the flat compressive anticrack analogue of Appendix C to an effective mixed-mode shear-compression criterion. The aim is to account for the fact that the weak layer may reach the onset of softening under a combined shear and compressive stress state, rather than under pure compression alone. We denote by  $\tau_g$  the applied shear load and by  $\sigma_g$  the applied slope-normal compressive load.

For consistency with the anticrack interpretation adopted in the main text, the collapsed region is treated as void-like and unsupported in both normal and tangential directions. We therefore set

$$\sigma_r = 0, \quad \tau_r = 0.$$

Thus, the residual/collapsed zone carries no normal support and no residual frictional shear resistance. Therefore the present approach does not apply to the case in which the slab comes into contact with the broken weak layer.

## D.1 Meaning of the affected-zone tip

As in the shear solution, we distinguish between the fully residual part of the weak layer and the full affected region. The length  $a_c$  denotes the end of the fully collapsed zone, whereas  $b_c$  denotes the leading edge of the affected region. Thus,

$$0 \leq x \leq a_c$$

is the collapsed zone,

$$a_c \leq x \leq b_c$$

is the finite softening zone, and

$$x \geq b_c$$

is the intact elastic zone.

The point  $x = b_c$  should therefore not be interpreted as the tip of a fully developed residual crack. It is the front of the process zone, where the weak layer first reaches the onset of softening. In the pure shear problem, this corresponds to

$$u(b_c) = u_p, \quad \tau(b_c) = \tau_p,$$

whereas at  $x = a_c$ ,

$$u(a_c) = u_r, \quad \tau(a_c) = \tau_r.$$

The mixed-mode construction below follows the same logic. At  $x = b_c$ , the local stress state reaches the mixed-mode peak surface, but neither the shear nor the normal component needs to reach its pure-mode peak value separately.

## D.2 Mixed-mode peak surface

We assume that the onset of local weak-layer softening is governed by an elliptical shear–compression peak surface,

$$\left(\frac{\tau}{\tau_p}\right)^2 + \left(\frac{\sigma}{\sigma_p}\right)^2 = 1,$$

where  $\tau_p$  is the pure shear peak strength and  $\sigma_p$  is the pure compressive collapse strength.

At the leading edge of the affected zone,  $x = b_c$ , we denote the local stress state by

$$\tau_{\text{tip}} = \tau(b_c), \quad \sigma_{\text{tip}} = \sigma(b_c).$$

The onset of mixed-mode softening is therefore written as

$$\left(\frac{\tau_{\text{tip}}}{\tau_p}\right)^2 + \left(\frac{\sigma_{\text{tip}}}{\sigma_p}\right)^2 = 1. \tag{69}$$

In pure compression,  $\tau_{\text{tip}} = 0$  and therefore

$$\sigma_{\text{tip}} = \sigma_p.$$

In mixed mode, however, the presence of shear generally implies

$$\sigma_{\text{tip}} < \sigma_p.$$

Thus,  $\sigma_{\text{tip}}$  is an unknown of the mixed-mode problem and must be solved together with the finite-softening anticrack matching equations.

### D.3 Normal anticrack field with unknown leading-edge stress

The slope-normal deflection  $w(x)$  is governed by

$$\mathcal{B}w'''' + \sigma(w) = \sigma_g,$$

where  $\mathcal{B}$  is the slab bending stiffness. The pre-peak normal stiffness is kept equal to its pure-mode value,

$$k_n = \frac{\sigma_p}{w_p},$$

where  $w_p$  is the normal displacement associated with the pure compressive peak strength. Therefore, if the leading edge of the affected zone reaches the normal stress  $\sigma_{\text{tip}}$ , the corresponding normal displacement is

$$w_{\text{tip}} = \frac{\sigma_{\text{tip}}}{k_n}.$$

We use a linear normal softening branch from  $\sigma_{\text{tip}}$  to zero over a normal softening distance  $\delta_n$ . This is the mixed-mode analogue of the scalar compressive softening law: the onset of softening occurs at  $x = b_c$ , where  $\sigma = \sigma_{\text{tip}}$ , and the collapsed unsupported state is reached at  $x = a_c$ . Thus,

$$k_s^{\text{tip}} = \frac{\sigma_{\text{tip}}}{\delta_n}.$$

The associated bending-softening length is

$$\ell_b^{\text{tip}} = \left( \frac{\mathcal{B}}{k_s^{\text{tip}}} \right)^{1/4} = \left( \frac{\mathcal{B}\delta_n}{\sigma_{\text{tip}}} \right)^{1/4}. \quad (70)$$

The intact bending-foundation length remains

$$\Lambda_b = \left( \frac{4\mathcal{B}}{k_n} \right)^{1/4}. \quad (71)$$

We define

$$\alpha = \frac{b_c - a_c}{\ell_b^{\text{tip}}}.$$

### D.4 Collapsed zone

In the collapsed zone,  $0 \leq x \leq a_c$ , the normal support vanishes, so

$$\mathcal{B}w_I'''' = \sigma_g.$$

With free-edge conditions

$$w_I''(0) = 0, \quad w_I'''(0) = 0,$$

the solution is

$$w_I(x) = A_0 + A_1x + \frac{\sigma_g}{24\mathcal{B}}x^4.$$

### D.5 Softening zone

In the softening zone,  $a_c \leq x \leq b_c$ , the normal support is assumed to decrease linearly from  $\sigma_{\text{tip}}$  at  $w = w_{\text{tip}}$  to zero at  $w = w_{\text{tip}} + \delta_n$ :

$$\sigma(w) = \sigma_{\text{tip}} - \frac{\sigma_{\text{tip}}}{\delta_n}(w - w_{\text{tip}}).$$

The governing equation becomes

$$\mathcal{B}w_{II}'''' - k_s^{\text{tip}}w_{II} = \sigma_g - \sigma_{\text{tip}} - k_s^{\text{tip}}w_{\text{tip}}.$$

A constant particular solution is

$$w_c = w_{\text{tip}} + \delta_n \frac{\sigma_{\text{tip}} - \sigma_g}{\sigma_{\text{tip}}}.$$

Thus,

$$w_{II}(x) = w_c + C_1 \cosh\left(\frac{x - a_c}{\ell_b^{\text{tip}}}\right) + C_2 \sinh\left(\frac{x - a_c}{\ell_b^{\text{tip}}}\right) + C_3 \cos\left(\frac{x - a_c}{\ell_b^{\text{tip}}}\right) + C_4 \sin\left(\frac{x - a_c}{\ell_b^{\text{tip}}}\right).$$

## D.6 Intact elastic zone

In the intact region,  $x \geq b_c$ ,

$$\mathcal{B}w_{III}'''' + k_n w_{III} = \sigma_g.$$

The bounded solution is

$$w_{III}(x) = \frac{\sigma_g}{k_n} + e^{-(x-b_c)/\Lambda_b} \left[ D_1 \cos\left(\frac{x - b_c}{\Lambda_b}\right) + D_2 \sin\left(\frac{x - b_c}{\Lambda_b}\right) \right].$$

## D.7 Matching at $x = a_c$

At  $x = a_c$ , the normal support has reached zero. The corresponding deflection is

$$w_r = w_{\text{tip}} + \delta_n.$$

Continuity of deflection, rotation, curvature and shear gives

$$w_I(a_c) = w_{II}(a_c) = w_r,$$

$$w_I'(a_c) = w_{II}'(a_c), \quad w_I''(a_c) = w_{II}''(a_c), \quad w_I'''(a_c) = w_{II}'''(a_c).$$

This yields

$$C_1 + C_3 = w_r - w_c = \delta_n \frac{\sigma_g}{\sigma_{\text{tip}}},$$

$$C_1 - C_3 = (\ell_b^{\text{tip}})^2 \frac{\sigma_g}{2\mathcal{B}} a_c^2,$$

$$C_2 + C_4 = \ell_b^{\text{tip}} \left( A_1 + \frac{\sigma_g}{6\mathcal{B}} a_c^3 \right),$$

and

$$C_2 - C_4 = (\ell_b^{\text{tip}})^3 \frac{\sigma_g}{\mathcal{B}} a_c.$$

Therefore,

$$C_1 = \frac{1}{2} \left[ \delta_n \frac{\sigma_g}{\sigma_{\text{tip}}} + (\ell_b^{\text{tip}})^2 \frac{\sigma_g}{2\mathcal{B}} a_c^2 \right],$$

$$C_3 = \frac{1}{2} \left[ \delta_n \frac{\sigma_g}{\sigma_{\text{tip}}} - (\ell_b^{\text{tip}})^2 \frac{\sigma_g}{2\mathcal{B}} a_c^2 \right],$$

$$C_2 = \frac{1}{2} \left[ \ell_b^{\text{tip}} \left( A_1 + \frac{\sigma_g}{6\mathcal{B}} a_c^3 \right) + (\ell_b^{\text{tip}})^3 \frac{\sigma_g}{\mathcal{B}} a_c \right],$$

and

$$C_4 = \frac{1}{2} \left[ \ell_b^{\text{tip}} \left( A_1 + \frac{\sigma_g}{6\mathcal{B}} a_c^3 \right) - (\ell_b^{\text{tip}})^3 \frac{\sigma_g}{\mathcal{B}} a_c \right].$$

## D.8 Matching at $x = b_c$

At  $x = b_c$ , the weak layer reaches the onset of mixed-mode softening. In terms of the normal component, this means

$$\sigma(b_c) = \sigma_{\text{tip}},$$

or equivalently

$$w_{II}(b_c) = w_{III}(b_c) = w_{\text{tip}} = \frac{\sigma_{\text{tip}}}{k_n}.$$

Define

$$S_0 = C_1 \cosh \alpha + C_2 \sinh \alpha + C_3 \cos \alpha + C_4 \sin \alpha,$$

$$S_1 = C_1 \sinh \alpha + C_2 \cosh \alpha - C_3 \sin \alpha + C_4 \cos \alpha,$$

$$S_2 = C_1 \cosh \alpha + C_2 \sinh \alpha - C_3 \cos \alpha - C_4 \sin \alpha,$$

$$S_3 = C_1 \sinh \alpha + C_2 \cosh \alpha + C_3 \sin \alpha - C_4 \cos \alpha.$$

Then

$$\begin{aligned} w_{II}(b_c) &= w_c + S_0, & w'_{II}(b_c) &= \frac{S_1}{\ell_b^{\text{tip}}}, \\ w''_{II}(b_c) &= \frac{S_2}{(\ell_b^{\text{tip}})^2}, & w'''_{II}(b_c) &= \frac{S_3}{(\ell_b^{\text{tip}})^3}. \end{aligned}$$

From  $w_{III}(b_c) = w_{\text{tip}}$ , one obtains

$$D_1 = w_{\text{tip}} - \frac{\sigma_g}{k_n} = \frac{\sigma_{\text{tip}} - \sigma_g}{k_n}.$$

Curvature continuity gives

$$D_2 = -\frac{\Lambda_b^2}{2} \frac{S_2}{(\ell_b^{\text{tip}})^2}.$$

The remaining normal matching conditions are therefore

$$S_0 + \delta_n \frac{\sigma_{\text{tip}} - \sigma_g}{\sigma_{\text{tip}}} = 0, \tag{72}$$

$$\frac{S_1}{\ell_b^{\text{tip}}} + \frac{1}{\Lambda_b} \frac{\sigma_{\text{tip}} - \sigma_g}{k_n} + \frac{\Lambda_b}{2} \frac{S_2}{(\ell_b^{\text{tip}})^2} = 0, \tag{73}$$

and

$$\frac{S_3}{(\ell_b^{\text{tip}})^3} - \frac{2}{\Lambda_b^3} \frac{\sigma_{\text{tip}} - \sigma_g}{k_n} + \frac{1}{\Lambda_b} \frac{S_2}{(\ell_b^{\text{tip}})^2} = 0. \tag{74}$$

Equation (73) is also useful for interpreting the bending-induced shear. It gives

$$\frac{S_1}{\ell_b^{\text{tip}}} = -\frac{\sigma_{\text{tip}} - \sigma_g}{k_n \Lambda_b} - \frac{\Lambda_b}{2} \frac{S_2}{(\ell_b^{\text{tip}})^2}.$$

Thus, the leading-edge rotation contains a contribution controlled by the intact bending-foundation length  $\Lambda_b$ , and a finite-softening correction involving the curvature-like quantity  $S_2$  and the bending-softening length  $\ell_b^{\text{tip}}$ .

## D.9 Tip shear stress

Slab bending induces a basal rotation. Under Euler–Bernoulli kinematics, the associated tangential displacement at the slab base is approximated by

$$u_{\text{bend}} \simeq \frac{h}{2} w'(b_c).$$

Using the pre-peak tangential stiffness

$$k_t = \frac{\tau_p}{u_p},$$

the bending-induced shear stress is

$$\tau_{\text{bend}} = k_t \frac{h}{2} w'(b_c) = \frac{\tau_p}{u_p} \frac{h}{2} \frac{S_1}{\ell_b^{\text{tip}}}. \quad (75)$$

Equivalently, using Eq. (73),

$$\frac{\tau_{\text{bend}}}{\tau_p} = -\frac{h}{2u_p} \left[ \frac{\sigma_{\text{tip}} - \sigma_g}{k_n \Lambda_b} + \frac{\Lambda_b}{2} \frac{S_2}{(\ell_b^{\text{tip}})^2} \right]. \quad (76)$$

The sign of this contribution depends on the adopted displacement convention. In the calculations reported here, the signed value is retained.

Since the collapsed region is assumed to be void-like in shear,  $\tau_r = 0$ . The shear stress at the leading edge of the affected zone is therefore estimated as

$$\tau_{\text{tip}} = \tau_g \left( 1 + \frac{b_c}{\Lambda} \right) + \tau_{\text{bend}}, \quad (77)$$

where

$$\Lambda = \sqrt{\frac{E' h u_p}{\tau_p}}$$

is the shear stress-transfer length. This expression is consistent with the flat limit: if  $\tau_g = 0$ , the shear-transfer contribution vanishes and the only remaining shear component is the bending-induced shear.

## D.10 Closed mixed-mode system

The finite-softening mixed-mode anticrack problem is reduced to four nonlinear equations for

$$A_1, \quad a_c, \quad \alpha, \quad \sigma_{\text{tip}}.$$

The first three equations are the normal matching conditions Eqs. (72)–(74). The fourth equation is the mixed-mode peak condition at the leading edge of the affected zone,

$$\left[ \frac{\tau_g \left( 1 + b_c / \Lambda \right) + \frac{\tau_p}{u_p} \frac{h}{2} \frac{S_1}{\ell_b^{\text{tip}}}}{\tau_p} \right]^2 + \left( \frac{\sigma_{\text{tip}}}{\sigma_p} \right)^2 = 1. \quad (78)$$

Once the system is solved,

$$b_c = a_c + \alpha \ell_b^{\text{tip}}.$$

This formulation recovers the pure compressive anticrack solution when the total shear contribution vanishes, i.e. when  $\tau_{\text{tip}} = 0$ , in which case  $\sigma_{\text{tip}} = \sigma_p$ . It also mirrors the logic of the shear solution:  $b_c$  is the leading edge of the process zone, where the peak surface is reached, while

$a_c$  is the trailing edge of the process zone, where the collapsed unsupported state is reached. The formulation remains an effective mixed-mode criterion because the normal and tangential fields are combined through the peak surface rather than obtained from a fully coupled vectorial weak-layer constitutive law. Nevertheless, the normal finite-softening field and the bending-induced shear are both obtained directly from the three-zone anticrack solution, without introducing an empirical bending-softening coefficient.

## Notation

Symbol	Meaning
$x$	Slope-parallel coordinate.
$z$	Vertical coordinate, positive upward, with $z = 0$ at the slab free surface and $z = -h$ at the slab-weak-layer interface.
$u(x)$	Slope-parallel weak-layer displacement.
$w(x)$	Slope-normal slab deflection in the anticrack extension.
$h$	Slab thickness.
$E'$	Plane-strain elastic modulus of the slab.
$E'h$	Axial stiffness of the slab per unit width.
$\sigma_{xx}$	Slope-parallel normal stress in the slab.
$\tau(x)$	Shear stress transmitted by the weak layer.
$\tau_g$	Gravitational shear stress acting on the slab.
$\tau_p$	Peak shear strength of the weak layer.
$\tau_r$	Residual shear strength of the weak layer.
$u_p$	Displacement at peak shear strength.
$u_r$	Displacement at residual shear strength.
$\delta = u_r - u_p$	Softening displacement in shear.
$a_c$	Critical crack length, i.e. half-length of the fully softened residual zone.
$b_c$	Critical propagation length, i.e. total half-length of the affected zone including the softening zone.
$\omega = b_c - a_c$	Fracture-process-zone length (or softening-zone length).
$\Lambda$	Elastic characteristic length of the slab-weak-layer system, defined by $\Lambda = \sqrt{E'h u_p / \tau_p}$ .
$\ell$	Shear softening length, defined by $\ell = \sqrt{E'h \delta / (\tau_p - \tau_r)}$ .
$\alpha$	Dimensionless softening-zone length, $\alpha = (b_c - a_c) / \ell$ .
$a_{c0}$	Brittle critical crack length obtained in the limit $\delta \rightarrow 0$ .
$C_a$	Dimensionless coefficient entering the small-softening approximation of $a_c$ .
$C_b$	Dimensionless coefficient entering the small-softening approximation of $b_c$ .
$u_I, u_{II}, u_{III}$	Displacement solutions in the residual, softening, and intact zones, respectively.
$\tau_I, \tau_{II}, \tau_{III}$	Shear stress solutions in the residual, softening, and intact zones, respectively.
$u_0$	Displacement at $x = 0$ in the residual-zone solution.
$u_c$	Constant particular solution in the softening zone for the shear problem.
$A, B$	Integration constants in the shear softening-zone solution.
$\rho$	Slab density.
$\ddot{u}_{\text{res}}$	Average slope-parallel acceleration in the residual zone used for the local dynamic correction in the DAMPM comparison.
$G_{IIc}$	Mode-II fracture energy associated with the linear softening law.

Symbol	Meaning
$\mathcal{B}$	Slab bending stiffness in the anticrack extension.
$\sigma(w)$	Slope-normal weak-layer support law in the anticrack extension.
$\sigma_g$	Gravitational normal stress acting on the slab.
$\sigma_p$	Peak compressive weak-layer strength in the anticrack extension.
$\sigma_r$	Residual compressive support in the anticrack extension.
$w_p$	Deflection at peak compressive support.
$w_r$	Deflection at residual compressive support.
$\delta_n$	Softening displacement in the normal/compressive mixed-mode extension.
$k_n$	Pre-peak compressive stiffness of the weak layer, $k_n = \sigma_p/w_p$ .
$k_t$	Pre-peak tangential stiffness of the weak layer, $k_t = \tau_p/u_p$ .
$k_s$	Tangent softening stiffness in compression, $k_s = (\sigma_p - \sigma_r)/\delta$ .
$k_s^{\text{tip}}$	Tangent softening stiffness in the mixed-mode anticrack formulation, $k_s^{\text{tip}} = \sigma_{\text{tip}}/\delta_n$ .
$\Lambda_b$	Bending-foundation characteristic length, $\Lambda_b = (4\mathcal{B}/k_n)^{1/4}$ .
$\ell_b$	Bending-softening length, $\ell_b = (\mathcal{B}\delta/(\sigma_p - \sigma_r))^{1/4}$ .
$\ell_b^{\text{tip}}$	Mixed-mode bending-softening length, $\ell_b^{\text{tip}} = (\mathcal{B}\delta_n/\sigma_{\text{tip}})^{1/4}$ .
$w_I, w_{II}, w_{III}$	Deflection solutions in the collapsed, softening, and intact zones of the anticrack extension.
$w_c$	Constant particular solution in the compressive softening zone.
$D_1, D_2$	Integration constants in the intact anticrack solution.
$C_1, C_2, C_3, C_4$	Integration constants in the softening-zone solution of the anticrack problem.
$S_0, S_1, S_2, S_3$	Matching combinations of $C_1, \dots, C_4$ evaluated at the leading edge of the softening zone.
$\tau_{\text{bend}}$	Shear stress induced by slab bending in the mixed-mode anticrack extension.
$\tau_{\text{tip}}$	Shear stress at the leading edge of the affected zone in the mixed-mode extension.
$\sigma_{\text{tip}}$	Normal stress at the leading edge of the affected zone in the mixed-mode extension.
$w_{\text{tip}}$	Normal displacement at the leading edge of the affected zone in the mixed-mode extension.
$C_a^{(b)}, C_b^{(b)}$	Dimensionless coefficients in the approximate finite-softening anticrack expressions for $a_c$ and $b_c$ .
$T$	Auxiliary notation in Appendix B, $T = \tau_p - \tau_g$ .
$R$	Auxiliary notation in Appendix B, $R = \tau_g - \tau_r$ .
$s$	Small parameter used in the asymptotic expansion, $s = \ell/\Lambda$ .
$m, n, p$	Coefficients in the asymptotic expansion of $\alpha$ in powers of $s$ .
$N_0$	Auxiliary quantity used in the asymptotic expansion of $a_c$ .

## References

- G. Bobillier, B. Bergfeld, J. Dual, J. Gaume, A. van Herwijnen, and J. Schweizer. Numerical investigation of crack propagation regimes in snow fracture experiments. *Granular matter*, 26(3):58, 2024.
- B. Chiaia, P. Cornetti, and B. Frigo. Triggering of dry snow slab avalanches: stress versus fracture mechanical approach. *Cold Reg. Sci. Technol.*, 53:170–178, 2008.

- J. Gaume, G. Chambon, N. Eckert, and M. Naaim. Influence of weak-layer heterogeneity on snow slab avalanche release: Application to the evaluation of avalanche release depths. *J. Glaciol.*, 59(215):423–437, 2013.
- J. Gaume, J. Schweizer, A. van Herwijnen, G. Chambon, B. Reuter, N. Eckert, and M. Naaim. Evaluation of slope stability with respect to snowpack spatial variability. *J. Geophys. Res.*, 119(9):1783–1789, 2014. doi: 10.1002/2014JF003193.
- J. Gaume, A. van Herwijnen, G. Chambon, K. Birkeland, and J. Schweizer. Modeling of crack propagation in weak snowpack layers using the discrete element method. *The Cryosphere*, 9: 1915–1932, 2015.
- J. Gaume, A. van Herwijnen, G. Chambon, N. Wever, and J. Schweizer. Snow fracture in relation to slab avalanche release: critical state for the onset of crack propagation. *The Cryosphere*, 11:217–228, 2017. doi: doi:10.5194/tc-2016-64.
- J. Gaume, T. Gast, J. Teran, A. van Herwijnen, and C. Jiang. Dynamic anticrack propagation in snow. *Nature Communications*, 9(1):3047, 2018.
- L. Guillet, L. Blatny, B. Trottet, D. Steffen, and J. Gaume. A Depth-Averaged Material Point Method for Shallow Landslides: Applications to Snow Slab Avalanche Release. *Journal of Geophysical Research: Earth Surface*, 128(8):e2023JF007092, 2023. ISSN 2169-9011. doi: 10.1029/2023JF007092.
- J. Heierli. *Anticrack model for slab avalanche release*. PhD thesis, Karlsruhe, Univ., Diss., 2008.
- J. Heierli, P. Gumbsch, and M. Zaiser. Anticrack nucleation as triggering mechanism for snow slab avalanches. *Science*, 321:240–243, 2008.
- P. Mahajan, R. Kalakuntla, and C. Chandel. Numerical simulation of failure in a layered thin snowpack under skier load. *Ann. Glaciol.*, 51(54):169–175, 2010.
- D. McClung. Direct simple shear tests on snow and their relation to slab avalanche formation. *J. Glaciol.*, 19(81):101–109, 1977.
- D. McClung. Shear fracture precipitated by strain softening as a mechanism of dry slab avalanche release. *J. Geophys. Res.*, 84(B7):3519–3526, 1979.
- F. Meloche, G. Bobillier, L. Guillet, F. Gauthier, A. Langlois, and J. Gaume. Modeling crack arrest in snow slab avalanches—toward estimating avalanche release sizes. *Journal of Geophysical Research: Earth Surface*, 130(12):e2025JF008470, 2025.
- F. Monti, J. Gaume, A. Van Herwijnen, and J. Schweizer. A simplified approach to assess the skier-induced stress within a multi-layered snowpack. *Nat. Hazard Earth Syst. Sci.*, 16, 2016.
- A. Palmer and J. Rice. The growth of slip surfaces in the progressive failure of over-consolidated clay. *Proc. R. Soc. London*, 332:527–548, 1973.
- A. M. Puzrin and L. Germanovich. The growth of shear bands in the catastrophic failure of soils. *Proceedings of the Royal Society A: Mathematical, Physical and Engineering Sciences*, 461(2056):1199–1228, 2005.
- A. M. Puzrin, T. Faug, and I. Einav. The mechanism of delayed release in earthquake-induced avalanches. *Proceedings of the Royal Society A: Mathematical, Physical and Engineering Sciences*, 475(2227), 2019.
- I. Reiweger. *Failure of weak snow layers*. PhD thesis, ETH Zurich, 2011.

- P. L. Rosendahl and P. Weissgraeber. Modeling snow slab avalanches caused by weak-layer failure—part 1: Slabs on compliant and collapsible weak layers. *The Cryosphere*, 14(1):115–130, 2020a.
- P. L. Rosendahl and P. Weissgraeber. Modeling snow slab avalanches caused by weak-layer failure—part 2: Coupled mixed-mode criterion for skier-triggered anticracks. *The Cryosphere*, 14(1):131–145, 2020b.
- J. Schöttner, M. Piecuch, M. Walet, P. Rosendahl, V. Adam, P. Weißgraeber, J. Schweizer, and A. van Herwijnen. Testing the strength of buried surface hoar weak layers under combined compression and shear loading. *Authorea Preprints*, 2025.
- J. Schweizer. Laboratory experiments on shear failure of snow. *Ann. Glaciol.*, 26:97–102, 1998.
- M. Siron, B. Trottet, and J. Gaume. A theoretical framework for dynamic anticrack and supershear propagation in snow slab avalanches. *Journal of the Mechanics and Physics of Solids*, 181:105428, 2023.
- B. Trottet, R. Simenhois, G. Bobillier, A. van Herwijnen, C. Jiang, and J. Gaume. Transition from sub-rayleigh anticrack to supershear crack propagation in snow avalanches. *Nature Physics*, page preprint, 2021. doi: <https://doi.org/10.21203/rs.3.rs-963978/v1>.
- J. C. Volmer, G. Anciaux, R. Peerlings, and J. Gaume. Modelling weak layer fracture using non-associated plasticity. MSc internship project report, École Polytechnique Fédérale de Lausanne and Eindhoven University of Technology, June 2017.
- P. Weissgraeber and P. L. Rosendahl. A closed-form model for layered snow slabs. *The Cryosphere*, 17(4):1475–1496, 2023.